Transport properties and thermoelectric effects in gated silicene superlattices

Cite as: J. Appl. Phys. **124**, 144305 (2018); https://doi.org/10.1063/1.5045479
Submitted: 20 June 2018 . Accepted: 22 September 2018 . Published Online: 11 October 2018

E. J. Guzmán, O. Navarro, O. Oubram, and I. Rodríguez-Vargas

Transport properties and thermoelectric effects in gated silicene superlattices

E. J. Guzmán,[1,2,a)] O. Navarro,[2] O. Oubram,[3] and I. Rodríguez-Vargas[4,b)]
[1]*Facultad de Ciencias Físico Matemáticas, Universidad Michoacana de San Nicolás de Hidalgo, Av. Francisco J. Mujica s/n Ciudad Universitaria, Morelia, Michoacán, Mexico*
[2]*Unidad Morelia del Instituto de Investigaciones en Materiales, Universidad Nacional Autónoma de México, Antigua Carretera a Pátzcuaro No. 8701, Col. Ex Hacienda de San José de La Huerta, 58190 Morelia, Michoacán, Mexico*
[3]*Facultad de Ciencias Químicas e Ingeniería, Universidad Autónoma Del Estado de Morelos, Av. Universidad 1001, Col. Chamilpa, 62209 Cuernavaca, Morelos, Mexico*
[4]*Universidad Autónoma de Zacatecas, Unidad Académica de Física, Calzada Solidaridad esquina con Paseo La Bufa s/n, CP 98060 Zacatecas, Zacatecas, Mexico*

(Received 20 June 2018; accepted 22 September 2018; published online 11 October 2018)

Low-dimensional thermoelectricity opens the possibility of improving the performance and the efficiency of thermoelectric devices by redistributing the electron density of states through the reduction of dimensionality. In this work, we explore this possibility in silicene by reducing its dimensionality through the periodic arrangement of gated electrodes, the so-called gated silicene superlattices. Silicene electrons were described quantum relativistically. The transmission, conductance, and thermoelectric properties were obtained with the transfer matrix method, the Landauer-Büttiker formalism, and the Cutler-Mott formula, respectively. We find that the redistribution of the density of states together with the intrinsic characteristics of silicene, the local bandgap and the large spin-orbit coupling, contribute to the enhancement of the thermoelectric properties. In particular, the Seebeck coefficient and the power factor reach values of a few mV/K and nW/K^2. These findings in conjunction with the low thermal conductivity of silicene indicate that silicene-based nanostructures could be the basis of more efficient thermoelectric devices. *Published by AIP Publishing.*
https://doi.org/10.1063/1.5045479

I. INTRODUCTION

In the last decade, research in 2D materials has grown enormously promoted by the extraordinary and exotic properties discovered in graphene.[1–3] Silicene is a graphene-like material formed by silicon (Si) atoms distributed in a honeycomb lattice.[4] In contrast to graphene, silicene possesses a low-buckled lattice attributed to mixed sp^2-sp^3 hybridization that results in the larger overlapping of the Si orbitals.[5] The buckling distance is about 0.44 Å.[6] Theoretical studies have shown that silicene is a semiconductor with a gap of 1.55 meV[7] whose charge carriers behave as Dirac massless fermions.[8] Freestanding silicene exhibits an intense spin-orbit coupling interaction of 3.9 meV,[9] which is useful for spin and valley manipulation of the carriers[10] and for the detection of quantum spin Hall effect.[7] Other exotic effects have also been predicted in silicene such as giant magnetoresistance[11,12] and chiral superconductivity.[13] In general, due to its outstanding properties and its natural compatibility with modern electronics, silicene is considered a promising material for future applications in nanotechnology.

Modern research in thermoelectricity could provide a solution to reduce the amount of heat wasted by society today. According to recent studies, the heat released to the environment represents more than 50% of the energy produced,[14] which is evidence of the low performance of modern thermal machines and electronic devices. Recovery of heat is possible according to the Seebeck effect,[15,16] which consists of the generation of a potential difference between two contacts by the existence of a temperature gradient. The conversion efficiency of a thermoelectric material is measured by the dimensionless quantity known as Figure of Merit $ZT = \sigma S^2 T/\kappa$,[17] where S is the Seebeck coefficient, σ is the electric conductance, T is the average absolute temperature, and κ is the thermal conductivity. The strategy to improve ZT is to reduce the thermal conductivity as much as possible while increasing the power factor σS^2. In bulk conventional materials, this is difficult to realize, since S, σ, and κ are interrelated according to Wiedemann-Franz law.[18] However, from the work of Hicks and Dresselhaus,[19] research in thermoelectricity has focused on low-dimensional materials or nanostructured systems, with the conjecture that higher ZT values could be found.[20,21] The reduction of dimensionality and the quantum confinement causes the redistribution of the density of states (DOS), which provide the opportunity to vary the power factor and thermal conductivity independently and thus be able to improve ZT. Today, the objective is to overcome the technological limit value $ZT = 3$ to develop more efficient devices that compete industrially.[22]

As expected, many theoretical studies of the thermoelectric effect in various graphene-based nanostructures have been carried out, reporting an improvement in thermoelectric

a)Electronic mail: jguzman@iim.unam.mx
b)Electronic mail: isaac@fisica.uaz.edu.mx

performance.[23] Following the same guideline, the study of thermoelectricity in other low-dimensional materials, like silicene, has grown significantly over the years. In particular, works on silicene nanoribbons (SiNRs) using *ab initio* numerical methods and density functional theory (DFT) have found high values of the Figure of Merit (ZT). Zberecki *et al.*[24] calculated a maximum value of $ZT \sim 2.5$ in zigzag SiNRs at 90 K. Pan *et al.*[25] obtained that SiNRs with hydrogen-passivated edges are structurally stable and reported a value superior of $ZT = 4.9$ at 600 K in the armchair case. Sadeghi *et al.*[26] showed that by introducing nanoporous and tuning the Fermi energy a value of $ZT \sim 3$ can be obtained, reaching a maximum of 3.5 over the temperature range 100 K-400 K. Yang *et al.*,[27] considering a nanostructure composed of silicon-germanium mixture found high ZT, up to 2.5, at room temperature. Here, it is important to remark that all these large values for the figure of merit are of theoretical nature and valid under the specific conditions in which they were derived. One of the major hurdles nowadays to assure or to be close to these outstanding values is the production of high quality silicene samples as well as the specific nanostructuration required in each case. Another type of nanostructure that has been extensively investigated is the so-called gated superlattices (GSLs). Previous works have explored the thermoelectric effects in graphene gated superlattices (GGSLs) and have found giant values of Seebeck coefficient and the power factor.[28–32] The possibility of building GSLs in silicene today is limited, since it has not been possible to synthesize silicene due to the instability of its buckled geometry. However, some experimental works have managed to deposit silicene in certain metallic substrates through epitaxial growth,[33–38] which can be exploited for the development of silicene-based electronic devices. For instance, Tao *et al.*[39] devised the synthesis-transfer-fabrication process of the silicene field-effect transistor. This process could be implemented and adapted to build GSLs on a silicene sheet.

In this paper, we have theoretically investigated the ballistic electronic transport and the thermoelectric effects in gated silicene-superlattices (GSSLs). Our model considers the Dirac-like Hamiltonian to describe the behavior of the carriers through the superlattice. This Hamiltonian includes the spin-orbit coupling and the on-site potential corresponding to low-buckled lattice of silicene. The electrostatic gated profile is introduced by a series of electrodes coupled to silicene sheet, which generates a superlattice of rectangular potential barriers alternated with potential wells. The transfer matrix method and Landauer-Büttiker formalism were used to calculate the transmission probability and conductance, respectively. The Seebeck coefficient and the power factor were obtained using the Cutler-Mott formula. We analyze the electronic transport and thermoelectric properties of each spin-valley component. We found that the conductance oscillations induced by the superlattice periodic potential give rise to maximums in the Seebeck coefficient and the power factor. In the K valley, the spin-down component dominates the thermoelectric properties, while in the K' valley the spin-up component does. The maximum values reached by the Seebeck coefficient and the power factor are in the order of mV/K and nW/K^2, respectively. Finally, we have confirmed that the redistribution of the density of states, induced by the reduction of the dimensionality of the GSSLs, is what improves the Seebeck coefficient and the power factor. This improvement in conjunction with the low thermal conductivity of silicene could be the base for the construction of more effective thermoelectric devices.

II. THEORETICAL MODEL FOR THE THERMOELECTRIC DEVICE BASED ON SILICENE SUPERLATTICES

The thermoelectric system that we have considered is a device formed by a sheet of silicene wrapped by a dielectric substrate on which a periodic series of metal electrodes is coupled, as shown schematically in Fig. 1(a). Through the electrodes, an external electrostatic field can be applied. The electrostatic potential profile is a periodic supperlattice formed by rectangular barriers and wells arranged in the direction of the x axis. Here, the strength of the potential barriers is U_b with width d_B and the wells have zero potential with width d_W. In Figs. 1(b) and 1(c) we show the potential profiles for the K and K′ valley, respectively. As we can notice the potential profile of the spin-up and spin-down components is not equivalent, in great extent, due to the on-site potential difference (Δ_z) caused by the low-buckled structure of silicene.

The silicene superlattice is joined at one end to a hot contact and at the other one to a cold contact. According to the Seebeck effect, the temperature difference generates an electric current through silicene, and thus a potential difference between the contacts can be measured.

To study the transport and thermoelectric properties in this device, we have considered the following low-energy effective Dirac Hamiltonian:[9,12]

$$H = \hbar v_F(p_x\tau_x - \eta p_y\tau_y) - (\sigma\eta\Gamma_{SO} - \Delta_z)\tau_z + UI, \quad (1)$$

where v_F is the Fermi velocity of the carriers in silicene, $\boldsymbol{p}$ is the canonical momentum vector, $\boldsymbol{\tau}$ represents the pseudospin Pauli matrices, I is the 2×2 unity matrix, $\sigma = \pm1$ denotes the electron spin property, $\eta = \pm1$ denotes the K and K' valleys of band structure of silicene, Γ_{SO} is the spin-orbit

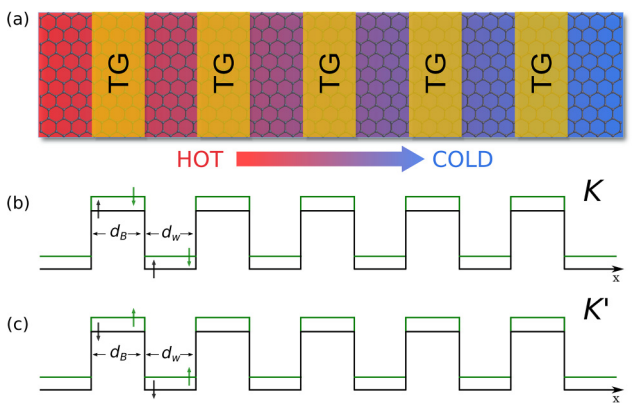

FIG. 1. (a) Schematic representation for thermoelectric silicene devices based on p-n junction superlattices. The arrow indicates the direction of the heat flow. Electrostatic potential profile for valleys (b) K and (c) K'. The green (clear) and black (dark) lines correspond to the down and up spin components in the case of K valley. For the K' valley, this correspondence is reversed.

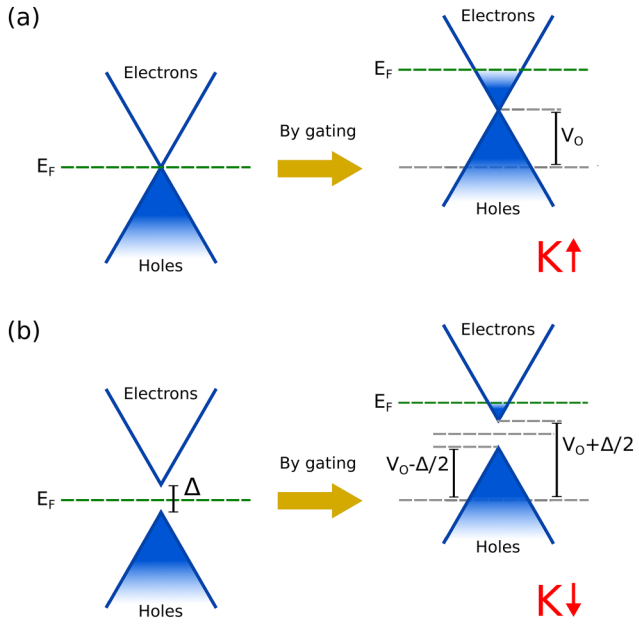

FIG. 2. Diagram of the silicene band structure for the (a) spin-up and (b) spin-down components of the K valley. For the K' valley, the band structure is similar; however, the spin components are reversed.

coupling energy, Δ_z is the on-site potential difference between two triangular sub-lattices which conform the hexagonal low-buckled lattice of silicene, and U describes the electrostatic profile of the superlattice. We have assumed well known values for the Fermi velocity and the spin orbit coupling energy:[9] $v_F = 0.5 \times 10^6$ m/s and $\Gamma_{SO} = 3.9$ meV. From now on, the quantities related to energy and length will be given in terms of $E_0 = 7$ meV and $L_0 = 81.1$ nm, respectively. These units of energy and length are typical in silicene studies.[11,12]

In Fig. 2, we show a diagram of the silicene band structure. Figures 2(a) and 2(b) correspond to the spin-up and spin-down components of the K valley, respectively. As $\Gamma_{SO} = \Delta_z$ the spin-up component is gapless, while the spin-down has a gap equal to $2\Delta_z$. In principle silicene is undoped, so the Fermi energy lies in between the valence and conduction band, left side of Figs. 2(a) and 2(b). By gating, it is possible to tune the Fermi energy as well as to shift the Dirac cones, right side of Figs. 2(a) and 2(b). By shifting the Dirac cones, we can create potential barriers. For the K' valley, the band structure is similar; however, the spin components are reversed. This band structure is distributed in the corners of the hexagonal Brillouin zone of silicene.

The corresponding eigenfunction for this Hamiltonian can be written in terms of incident and reflected waves as follows:

$$\psi_j(x, y) = \left[A_j \begin{pmatrix} 1 \\ \upsilon_j^+ \end{pmatrix} e^{ik_{x,j}x} + B_j \begin{pmatrix} 1 \\ \upsilon_j^- \end{pmatrix} e^{-ik_{x,j}x}\right] e^{ik_y y}, \quad (2)$$

where the index j indicates the wave function of the barrier (B) and well (W) zone, respectively. Additionally, the coefficients of the bispinor functions are given as

$$\upsilon_j^{\pm} = -\frac{(E - U_j) + (\sigma\eta\Gamma_{SO} - \Delta_{z,j})}{\pm k_{x,j} + i\eta k_y}. \quad (3)$$

Here, we must remember that the well has a zero electrostatic potential, i.e., $U_W = 0$. The components of the wave vector for each case are given by

$$k_{x,j} = \sqrt{(E - U_j)^2 - (\sigma\eta\Gamma_{SO} - \Delta_{z,j})^2 - k_y^2}, \quad (4)$$

and $k_y = k_F^* \sin\theta$, where $k_F^* = \sqrt{E^2 - (\sigma\eta\Gamma_{SO} - \Delta_{z,W})^2}$ is the dimensionless magnitude of the Fermi wave-vector and θ is the angle of incidence of the electrons in the x–y plane.

To relate the unknown coefficients A_j and B_j of the right and left semi-infinite regions, we require to use the continuity condition of the wave function employed for each well-barrier interface as well as the conservation of k_y. Thus, using the standard transfer matrix method we can connect the input state with the output state, i.e.,

$$\begin{pmatrix} A_{in} \\ B_{in} \end{pmatrix} = M_T^{(N)} \begin{pmatrix} A_{out} \\ 0 \end{pmatrix}, \quad (5)$$

where the total transfer matrix $M_T^{(N)}$ for N-period superlattice is given by

$$M_T^{(N)} = [M_B M_W]^N M_W^{-1}, \quad (6)$$

where $M_B = D_W^{-1}(D_B P_B D_B^{-1}) D_W$ and $M_W = D_W^{-1}(D_W P_W D_W^{-1}) D_W$, which are described in terms of the dynamic matrix

$$D_j = \begin{pmatrix} 1 & 1 \\ \upsilon_j^+ & \upsilon_j^- \end{pmatrix}, \quad (7)$$

and propagation matrix

$$P_j = \begin{pmatrix} e^{-ik_{x,j}d_j} & 0 \\ 0 & e^{ik_{x,j}d_j} \end{pmatrix}, \quad (8)$$

where the index j represents both barrier (B) and well (W) cases.

We can calculate the quantum probability transmission coefficient using the following expression:

$$T_{\sigma,\eta}(E, \theta) = \frac{1}{\left|M_T^{(N)}(1, 1)\right|^2}, \quad (9)$$

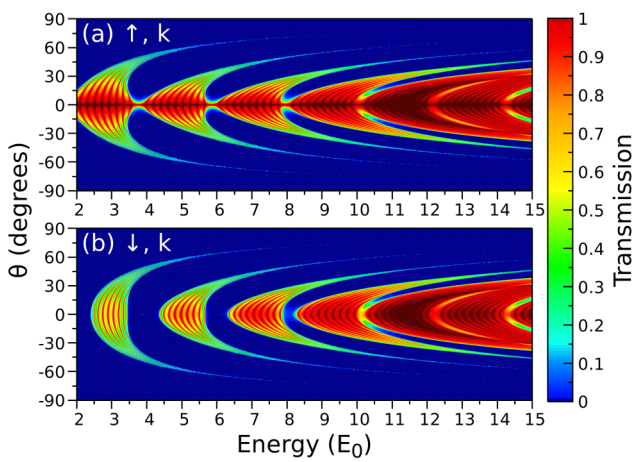

FIG. 3. Transmission probability as a function of energy and the angle of incidence for the GSSLs structure for two different conduction channels: (a) *up-K* and (b) *down-K*. The structure is formed by 10 barriers with potential $U_B = 5$ and width $d_B = 0.5$, where the width of the wells is $d_W = 1.0$.

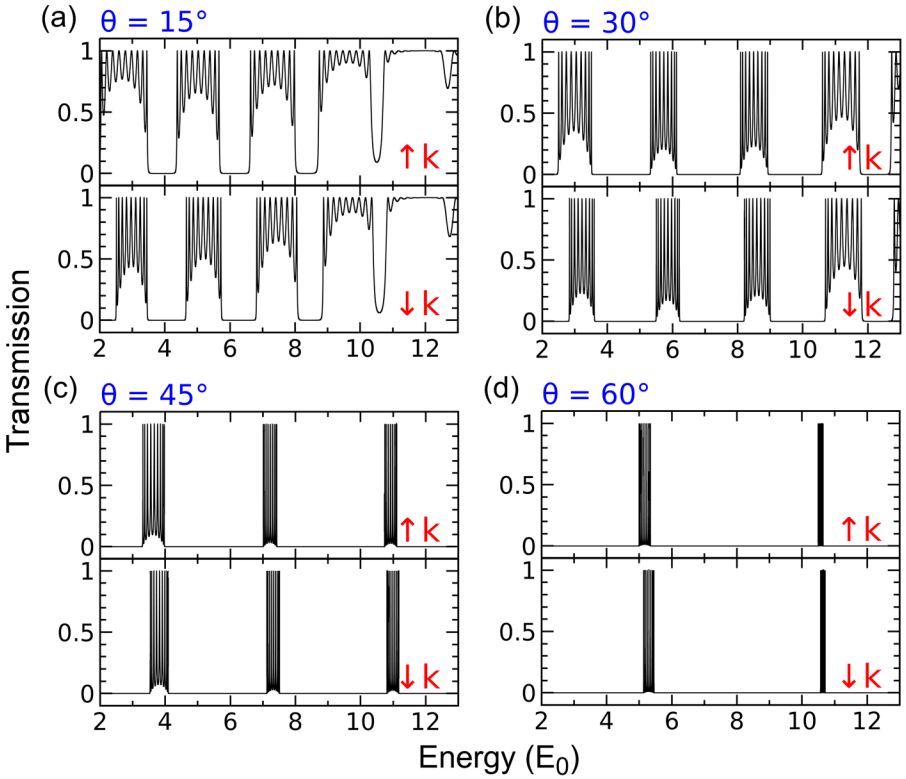

FIG. 4. Transmission probability as a function of the energy for different angles of incidence: (a) 15°, (b) 30°, (c) 45°, and (d) 60° both for the *up-K* channel and for the *down-K* channel. The parameters of the superlattice are the same as in Fig. 3.

where σ and η denotes the spin and valley channel, respectively.

The energy band structure can be obtained from the dispersion relationship which relates mathematically the wave vector of the supperlattice with the trace of the unit-cell transfer matrix (barrier plus well), i.e.,

$$\begin{aligned}\cos(q_{SL}d_{SL}) &= \frac{1}{2}\mathrm{Tr}\left[D_B P_B D_B^{-1}\cdot D_W P_W D_W^{-1}\right]\\ &= \cos(k_{x,B}d_B)\cos(k_{x,W}d_W)\\ &\quad - \Xi\sin(k_{x,B}d_B)\sin(k_{x,W}d_W),\end{aligned} \tag{10}$$

where

$$\Xi \equiv \frac{E(E-U_B)-(\sigma\eta\Gamma_{SO}-\Delta_{z,B})(\sigma\eta\Gamma_{SO}-\Delta_{z,W})-k_y^2}{k_{x,B}k_{x,W}}. \tag{11}$$

The unit cell length is $d_{SL}=d_B+d_W$, and q_{SL} is the Bloch wave vector characteristic of an infinite periodic supperlattice.

Additionally, if we know the band structure, we can derive the density of states (DOS) of the system, which is mathematically given by the following equation:

$$DOS_{\sigma,\eta}(E,\theta)=\frac{1}{2\pi}\left|\frac{\partial q_{SL}(E,\theta)}{\partial E}\right|. \tag{12}$$

By summing over all angles, we obtain the integrated density of states $DOS_{\sigma,\eta}(E)$. And by considering the contribution of both valleys and both spins, we get the global density of states $DOS(E)$.

The Landauer-Büttiker formalism provides a way to calculate the ballistic transport. In this framework, the conductance for an individual type of electronic channel (η, σ) is given as follows:

$$\begin{aligned}G_{\sigma,\eta}(E_F) &= \frac{e^2}{h}\sum_{k_y}T_{\sigma,\eta}(E_F,k_y)\\ &= G_0 k_F^*\int_{-\pi/2}^{\pi/2}T_{\sigma,\eta}(E_F,k_F\sin\theta)\cos\theta\,d\theta,\end{aligned} \tag{13}$$

where $G_0=e^2L_yE_0/h^2v_F$, with L_y the width of the silicene sheet in the transverse y-coordinate. We have taken a typical value of 200 nm for this structural parameter. The global conductance is simply the sum of the four conduction channels, i.e., $G=\sum_{\eta,\sigma}G_{\sigma,\eta}$.

In order to analyze the thermoelectric effect in this system, the calculation of the Seebeck coefficient is required. This crucial quantity can be written in the linear response approximation as

$$S=-\frac{\Delta V}{\Delta T}=\frac{G_S}{G}, \tag{14}$$

where

$$G=\int_{-\infty}^{+\infty}G(E)\left(-\frac{\partial f}{\partial E}\right)dE, \tag{15}$$

$$G_S=\int_{-\infty}^{+\infty}G(E)\left(-\frac{\partial f}{\partial E}\right)\left(\frac{E-\mu}{eT}\right)dE, \tag{16}$$

with T and μ the average (equilibrium) temperature and chemical potential and f the Fermi distribution function. By considering that $\partial f/\partial E$ is a peaked function around E_F, we can carry out the so-called Sommerfeld expansion by developing $G(E)$ in a Taylor series around E_F. By keeping the dominant terms and calculating the corresponding integrals,

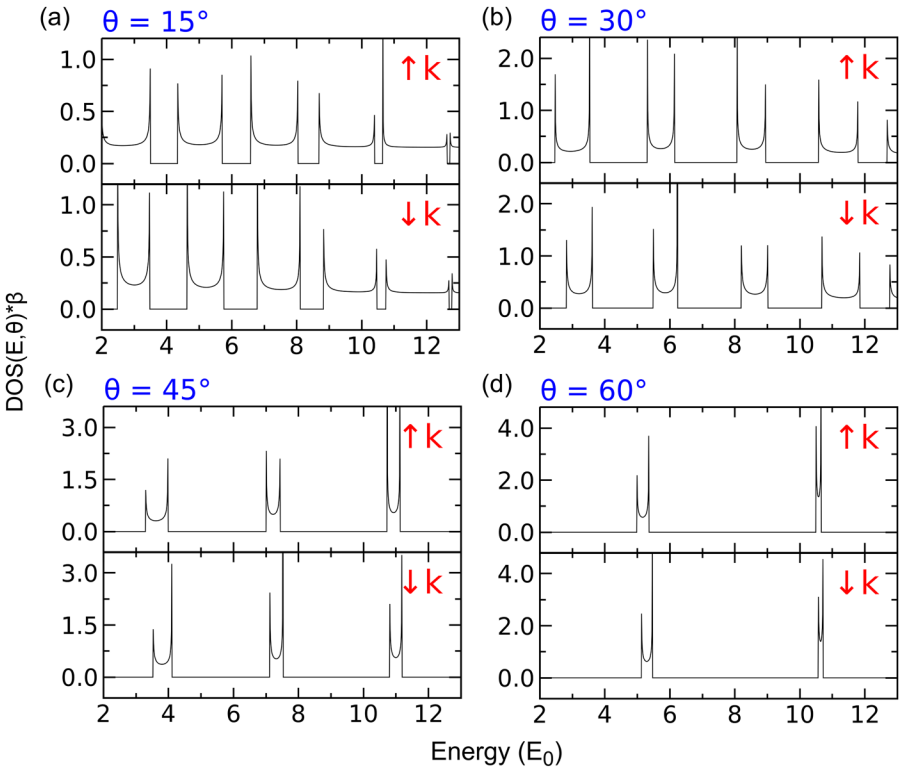

FIG. 5. Density of states as a function of energy for different angles of incidence: (a) 15°, (b) 30°, (c) 45°, and (d) 60° both for the *up-K* channel and for the *down-K* channel. The parameters of the superlattice are the same as in Fig. 3, and β is equal to v_F. So, the vertical axis represents simply the number of states.

we can arrive to the following expressions:

$$G = G(E_F), \tag{17}$$

$$G_S = \frac{\pi^2 k_B^2 T}{3e} G^{(1)}(E_F), \tag{18}$$

where $G^{(1)}(E_F)$ represents the first derivative of $G(E)$ evaluated at the Fermi energy. By substituting these expressions in Eq. (14), we obtain the well-known Cutler-Mott formula:[40]

$$S(E) = \frac{\pi^2 k_B^2 T}{3e} \frac{\partial[\ln G(E)]}{\partial E}\bigg|_{E=E_F}. \tag{19}$$

In the present study, we have considered $T = 50$ K. This election is twofold, first to assure the validity of the Cutler-Mott relation in 2D materials[41] and second to be in a reasonable range of quantum coherent transport.[42] For the case of a single spin-valley channel, the Seebeck coefficient is calculated by substituting the global conductance G for $G_{\sigma,\eta}(E)$.

The power factor is a quantity that results from the product between the squared magnitude of the Seebeck coefficient and the conductance, i.e., S^2G. High values of this factor directly improve the efficiency of the device in the conversion of heat into electrical energy, here is where its importance lies.

III. NUMERICAL RESULTS

We have carried out a systematic study which consists of the calculation of transport properties such as transmission and conductance as well as the calculation of thermoelectric properties such as the Seebeck coefficient and the power factor for N-period GSSLs. The intrinsic characteristics of

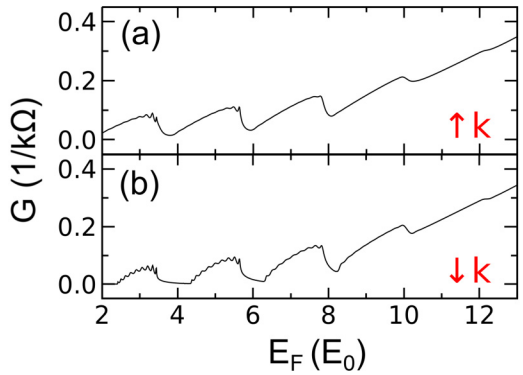

FIG. 6. Conductance as a function of energy for the GSSLs structure and for two different conduction channels: (a) *up-K* and (b) *down-K*. The structure is formed by 10 barriers with potential $U_B = 5$ and width $d_B = 0.5$. The width of the wells is $d_W = 1.0$.

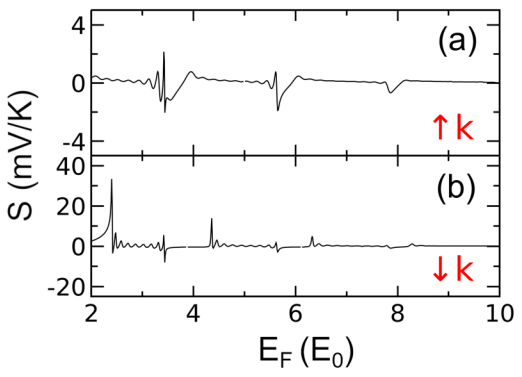

FIG. 7. Seebeck coefficient as a function of energy for the GSSLs structure and for two different conduction channels: (a) *up-K* and (b) *down-K*. The parameters of the superlattice are the same as in Fig. 6.

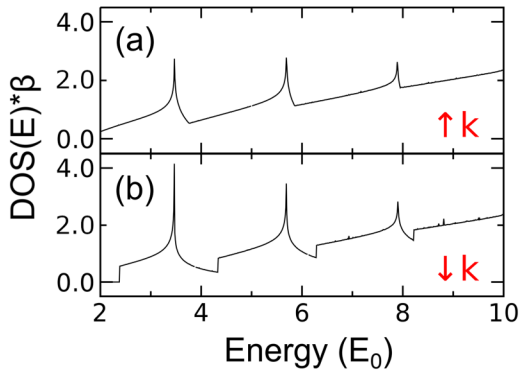

FIG. 8. Density of states as a function of energy for the GSSLs structure and for two different conduction channels: (a) *up-K* and (b) *down-K*. The parameters of the superlattice are the same as in Fig. 6 and β is equal to v_F.

silicene allow us to discriminate the behaviour between the spin-valley channels (σ, η), an advantage over graphene itself. Also, we have obtained the density of the states of the system which helps us to explain the connection between the transport and thermoelectric phenomena.

In our full study, we only consider GSSLs formed by 10 rectangular barriers with potential $U_B = 5$ and width $d_B = 0.5$, which are separated by zero potential wells of width $d_W = 1.0$. The on-site potential difference is $\Delta_z = \Gamma_{SO} = 0.56$ throughout the structure ($\Delta_{z,B} = \Delta_{z,W}$). The widths for barriers and wells are typical values used in the literature.[11,12] These values are also appropriate if we want to incorporate magnetic barriers.[11,12] Furthermore, these values lie in the range of the reported widths for electrostatic barriers in 2D materials.[42] In Fig. 3, it is shown a color map (contour) of the transmission as a function of the energy and the angle of incidence for the GSSLs structure both for the case of *up-K* channel [Fig. 3(a)] and for the *down-K* channel [Fig. 3(b)]. As we can see in the maps, the transmission contains very marked areas with certain propagation probability, where we highlight tunneling areas (red zones) and areas where propagation is impossible (blue zones) or bandgaps. At $T_{\sigma,\eta} = 1$, the superlattice is practically invisible (transparent) for carriers, such an effect is a result of Fabry-Pérot resonances inside the wells, in contrast to the gaps ($T_{\sigma,\eta} = 0$), where the interference is destructive. The transmission

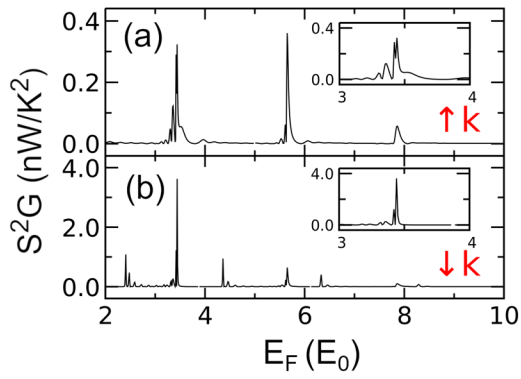

FIG. 9. Power factor as a function of energy for the GSSLs structure and for two different conduction channels: (a) *up-K* and (b) *down-K*. The parameters of the superlattice are the same as in Fig. 6.

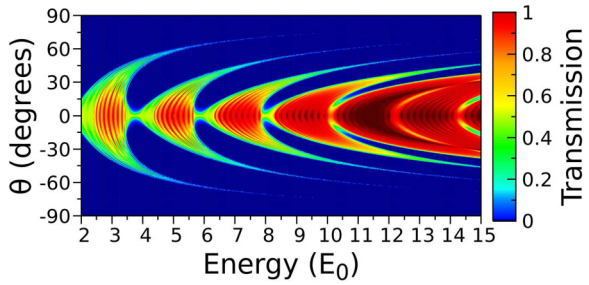

FIG. 10. Global transmission probability as a function of energy and the angle of incidence for the GSSLs structure. The structure is formed by 10 barriers with potential $U_B = 5$ and width $d_B = 0.5$, where the width of the wells is $d_W = 1.0$.

contour is composed of bands in the form of branches concentrated around the normal angle, here it is where the highest probability of propagation is found. With the angle of incidence the bands narrow, the transmission decreases and the forbidden zones (gaps) grow. In addition, we have obtained a clear difference in transmission between the spin-valley channels, which provides the possibility of choosing a specific type of current, and thus to be able to modulate the transport and thermoelectric properties of this system. It is important to mention that the results of the transmission for *up-K′* and *down-K′* are identical to those obtained for *down-K* and *up-K*, respectively. So, it is not necessary to present them explicitly in this paper. This similarity comes from the equivalence of the wave vector between these spin-valley channels.

In Fig. 4, it is shown the transmission versus energy for different angles of incidence: 15°, 30°, 45°, and 60° for the 10-period GSSLs structure and both for the *up-K* channel and for the *down-K* channel. Note that these results are horizontal cutoffs in Fig. 3 for each angle case. In this figure, we can see the energy miniband structure is formed by propagating regions ($T_{\sigma,\eta} \neq 0$) separated by gaps ($T_{\sigma,\eta} = 0$). Note that there is a clear difference in the band structure between both spin-valley conduction channels, a crucial aspect for applications in valley-spintronics. It is important to highlight that the minibands distribution is significantly modified with the change of the angle of incidence. In fact, as the angle increases the width of the minibands narrows and the width of the gaps widens, leading to a drastic change in transmission at the edges between allowed minibands and the gaps.

In Fig. 5, it is shown the density of states as a function of energy for the same angles and spin-valley components as in the previous figure. The vertical axis represents simply the number of states, since the parameter $\beta = \hbar v_F$ has units of energy and distance. In the middle of the permitted regions, a finite number of states were found, while into the gaps there are no states available as we expected. However, the aspect that we most appreciate is the accumulation of a large number of states at the edges between the available regions and the gaps. Additionally, we can see that the accumulation of states increases up to four times as the incident angle grows from 15° to 60°. Also, the width of the regions of allowed states is reduced in accordance with the transmission bands. As we will see later, summing over all angles will

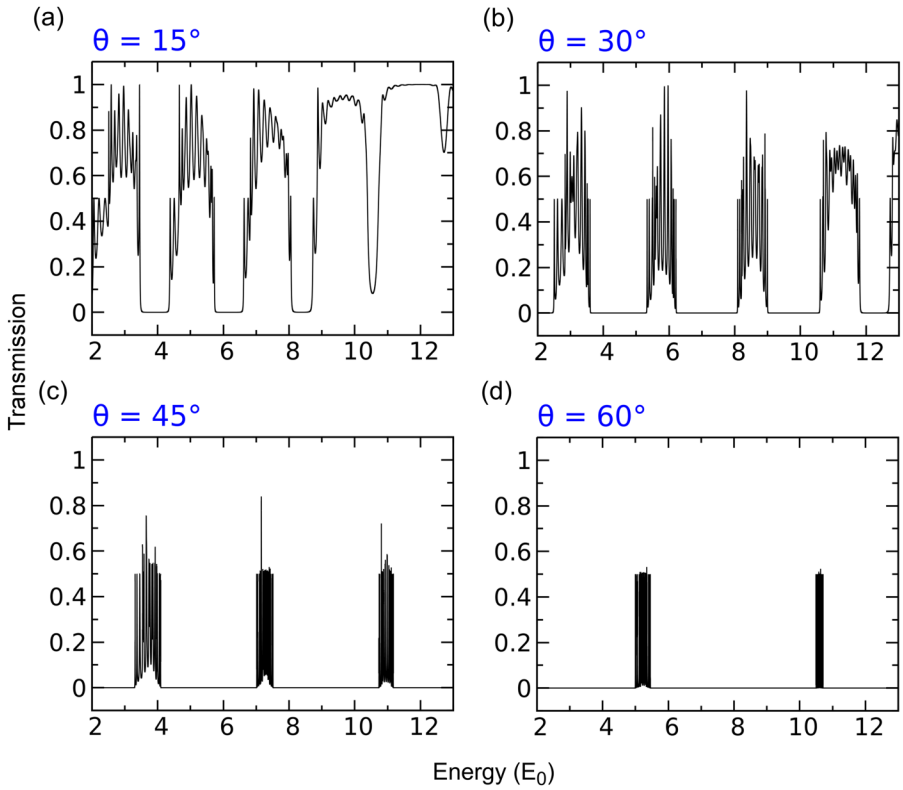

FIG. 11. Global transmission probability as a function of energy for different angles of incidence: (a) 15°, (b) 30°, (c) 45°, and (d) 60°. The parameters of the superlattice are the same as in Fig. 10.

result in $DOS_{\sigma,\eta}(E)$ with accumulation of states at preferential energies, and as a consequence to the improvement of the thermoelectric properties.

In order to obtain results that involve measurable and comparable quantities with experiments, we have considered the calculation of conductance, which is a quantity that counts the contribution of the transmitted carriers, that move in all directions, to the total current flowing through the device. In Fig. 6, we show the conductance for the 10-period GSSLs structure and for *up-K* and *down-K* channels. In this figure, below a certain energy level ($E < 9$), the conductance is an oscillating curve formed by high-conduction zones alternated with low-conduction zones. In this energy range, there is a clear difference in conductance between the two

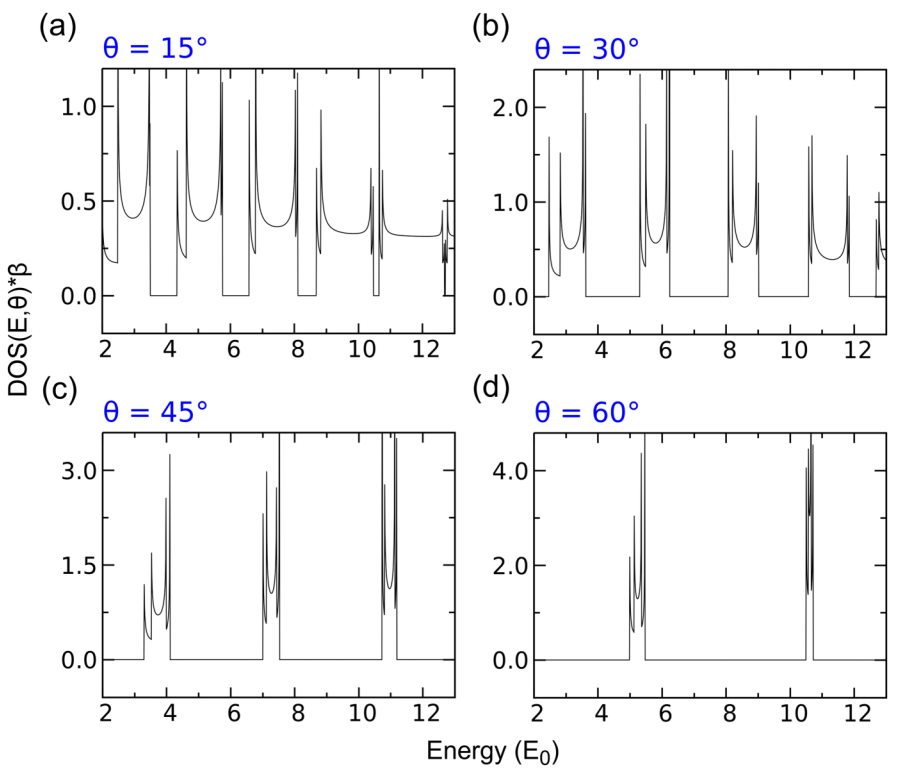

FIG. 12. Global density of states as a function of energy for different angles of incidence: (a) 15°, (b) 30°, (c) 45°, and (d) 60°. The parameters of the superlattice are the same as in Fig. 10, and β is equal to v_F.

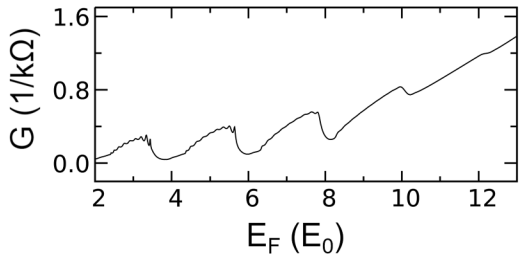

FIG. 13. Global conductance as a function of energy for the GSSLs formed by 10 barriers with potential $U_B = 5$ and width $d_B = 0.5$. The width of the wells is $d_W = 1.0$.

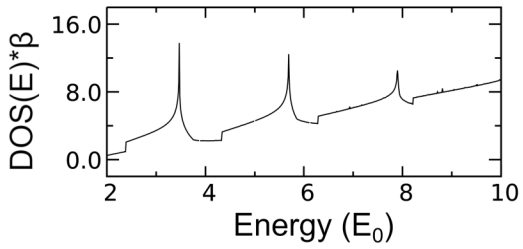

FIG. 15. Global density of states as a function of energy for the GSSLs. The parameters are the same as in Fig. 13 and β is equal to v_F.

channels, for the case of *up-K* channel the small oscillations localized into high-conduction zones are smooth while in the case of *down-K* channel they are more pronounced. In addition, we can notice that as the energy of the carriers grows ($E > 9$) the superlattice potential becomes irrelevant, and consequently $T_{\sigma,\eta}$ will tend to 1. Then, according to Eq. (13), the conductance will be proportional to the Fermi energy as well as the same for both channels.

As it is expected, drastic changes in transport will improve the thermoelectric properties. In Fig. 7, we ratify this fact with the calculation of the Seebeck coefficient from the conductance using Eq. (14), where we substitute G by $G_{\sigma,\eta}$. Our results show that the maximum values of the Seebeck coefficient are located in the limits between low and high-conduction regions. Here, we emphasize that the values obtained for the *down-K* channel are up to one order of magnitude higher than for the *up-K* channel. For both spin components, the Seebeck coefficient reaches values of the order of mV/K. The appearance of the peaks in the Seebeck coefficient is associated with the redistribution of the states by reducing the dimensionality of the system. Figure 8 presents the DOS as a function of energy for both the *up-K* channel and the *down-K* channel. For the *up-K* channel case, we can see that the density of states has an increasing trend with energy regions of high accumulation of states. We can also appreciate that the accumulation of states occurs precisely at energy regions at which the Seebeck coefficient is maximum. For the *down-K* channel, in addition to the mentioned trend of the DOS for the *up-K* channel, we can see a small bandgap at the low energy side ($E < 2.4$) and energy zones with abrupt changes in the DOS. In these energy zones is where we find the maximum values of the Seebeck coefficient, see Fig. 7. Finally, the combination of conductance and high Seebeck coefficient will be reflected in the improvement of the power factor, as shown in Fig. 9. The maximum power factor observed in the *up-K* channel is around 0.35 nW/K^2, while in the *down-K* channel is about 3.5 nW/K^2, then it is ten times higher than in the other channel. So, the greater this factor, the higher the Figure of Merit and therefore a better thermoelectric efficiency, since these quantities are closely related.

Now, we consider an analogous study to the proceeding for valley-spin components, but now for the case of global transport. Figure 10 shows a color map of the transmission as a function of the energy and angle of the incident carriers for GSSLs consisting of 10 barriers with potential energy $U_B = 5$ and width $d_B = 0.5$, where the width of the wells is $d_W = 1.0$. In this case, the transmission is calculated as the average of the four spin-valley channels, i.e., $\overline{T} = \frac{1}{4}\sum_{\sigma,\eta} T_{\sigma,\eta}$. The global transmission is $\overline{T} = \frac{1}{2}\left(T_{\uparrow,K} + T_{\downarrow,K}\right)$, since the transmission of the *up-K* and *down-K* channels is equal to the transmission of the *down-K′* and *up-K′* channels, respectively. In Fig. 10, it is observed that the global transmission zone includes the union of the transmission zones of both channels, obtaining a greater extension than the individual parts. The global transmission is balanced in most of the zones, that is, decrease in areas of high transmission and grew in areas of low transmission, even where there were gaps. Also, there are transmission zones that maintained their value due to the fact that they are equivalent in both channels. An important point is that the global transmission maintains a structure similar to the transmission obtained individually for each channel, formed by transmission bands that are concentrated around the normal angle and whose amplitude decreases when the angle grows. Figure 11 shows the transmission probability versus energy for the GSSLs structure and for different incident angles of the carriers: 15°, 30°, 45°, and 60°. Note that these minibands profiles are horizontal cutoffs of transmission of Fig. 10 for each angle case. In Fig. 11, we can notice that as

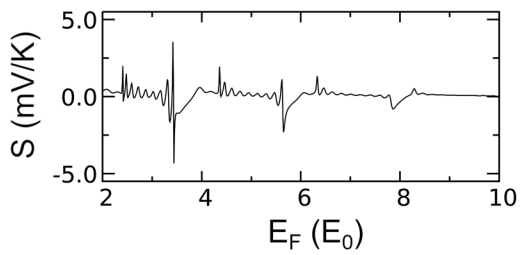

FIG. 14. Seebeck coefficient as a function of energy for the GSSLs. The parameters are the same as in Fig. 13.

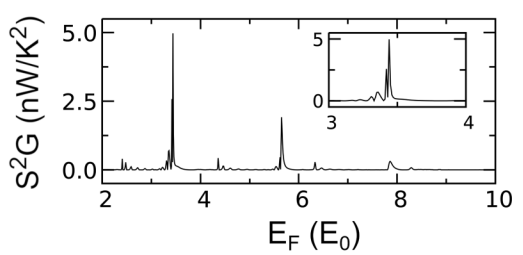

FIG. 16. Power factor as a function of energy for the GSSLs. The parameters are the same as in Fig. 13.

the angle of incidence increases the width of the bands is reduced and consequently the gaps are enlarged. Similarly, for large angles (60°), the value of the transmission is affected and falls to around 0.5. This interplay between the spin-valley components is also reflected in $DOS_{\sigma,\eta}(E, \theta)$, see Fig. 12. As in the case of individual spin-valley components, there are regions of available states that correspond to transmission bands, while the transmission gaps have no available states. We can also notice that the accumulation of states is taking place at the edges of the minibands, however, in this case an additional peak is induced by the interplay between the spin-valley components. This reshaping of the distribution of states will affect the global $DOS(E)$ as well as the transport and thermoelectric properties.

In Fig. 13, we show the global conductance as a function of energy for the 10-period GSSLs. As we mentioned in Sec. II, the global conductance is simply the sum of the four conduction channels, i.e., $G = 2(G_{\uparrow,K} + G_{\downarrow,K})$, where the factor 2 is due to the equality between the channels *up-K* (*down-K*) and *down-K′* (*up-K′*). In this figure, we can see for $E < 9$ that the conductance has the shape of an oscillating curve formed by zones of low and high-conduction which alternate in the direction of the energy axis, while for high energies the conductance increases linearly with k_F. In addition, we can notice the presence of small pronounced conductance oscillations inside the zones of high-conduction. The abrupt changes in the conductance are reflected in high values of the Seebeck coefficient as shown in Fig. 14, where the high values of the Seebeck coefficient are located in the limits between low and high-conduction zones. The maximum value is 4 mV/K, which is greater than the value obtained in the *up-K* channel (2 mV/K) and less than the value obtained in the *down-K* channel (35 mV/K). Figure 15 presents the global DOS as a function of energy which counts the total number of states due to the factor $\beta = \hbar v_F$. The global DOS has a similar pattern as the DOS for the *down-K* channel, that is, energy regions with high accumulation of states, a small bandgap at low energies and energy zones with abrupt changes. This redistribution of the states is the origin of the maximum values of the Seebeck coefficient observed in Fig. 14. The peaks of the Seebeck coefficient are responsible for improving the power factor as seen in Fig. 16, and therefore increase the efficiency of the system to convert heat into electric energy. In Fig. 16, we found a value of power factor of approximately 5 nW/K^2, greater than the value obtained both for the *up-K* channel (0.35 nW/K^2) and for the *down-K* channel (3.5 nW/K^2) individually.

IV. DISCUSSION

In this section, we will discuss some relevant aspects about our results as well as others, such as the silicene thermal conductivity, directly related to the efficiency of a possible thermoelectric device based on GSSLs.

In first place, we want to remark that the obtained values for the Seebeck coefficient and the power factor, of the order of mV/K and nW/K^2, respectively, are only possible if very specific conditions are met. The following are considered as fundamental:

- It is necessary that the electronic transport be of ballistic nature, that is, that the transport characteristic be a pure manifestation of coherent quantum interference. The main condition to assure this transport regime is that the mean free path of the charge carriers be larger than the length of the device. The extraordinary mean free path of 2D materials makes that this regime be totally reachable. For instance, in graphene mean free paths of 15 μm at low temperature and of 1 μm at room temperature are reported.[43] In fact, unprecedented phenomena like Klein tunneling,[42] atomic collapse,[44] negative refraction,[45] and size quantization[46] in graphene owe its experimental verification to coherent quantum interference. In silicene, the electron mean free path is shorter than in graphene but still very large.[47] Besides, the continuous refinement of the growth processes and patterning techniques make plausible that in the near future we can think in coherent quantum transport in a wide range of temperatures. Furthermore, this transport regime assures that scattering by impurities, imperfections, and phonons have a limited role. We are also considering that the periodic potential varies slowly in the scale of the interatomic distances of silicene, so it does not constitute a source of valley-spin scattering.[48] Here, it is also important to mention that even when the spin-orbit interaction is stronger in silicene than in graphene, we are not considering it as strong as in germanene or transition metal dichalcogenides to represent a source of valley-spin scattering.[49]
- The potential barriers have to be as sharp as possible, otherwise effects such as collimation will dominate the transmission across the barriers. In fact, it is well known that smooth potential junctions leads to collimation, that is, the transmission of charge carriers is only possible at normal and nearly normal incidence.[50] So, our results cannot be reproduced by smooth potentials because the transmission minibands, which are the key, are well defined at oblique incidence. Fortunately, nowadays the refinement of the fabrication techniques of pn junctions allows sharp potentials. In fact, negative refraction in graphene has been possible due to the improvement of the mentioned techniques.[45] In silicene, these techniques are under way. Nowadays, there is a fabrication technique for field effect transistors,[39] and in principle the same patterning process for metallic contacts can be used to obtain potential barriers. So, we can think that sooner or later sharp potentials will be possible in silicene too.

In second place, we want to talk about the spin-orbit interaction. Although this interaction remains fixed throughout the study, it has important consequences in practically all relevant quantities: transmission, density of states, conductance, Seebeck coefficient, and power factor. The main effect of the spin-orbit coupling, in conjunction with Δ_z, is a gapless band structure for the spin-up component of the K valley and a gapped one for the spin-down component of the same valley, see Figs. 2(a) and 2(b). For the K' valley, the roles between the spin components are reversed. This differentiation between the spin components affects all transport and thermoelectric properties. For instance, the spin-down component of the density of

states presents a gap at the low energy side and the corresponding conductance curve turns out steeper, see Figs. 6 and 8. These characteristics improve and dictate in great extent the total thermoelectric properties, in other words, the spin-down component is dominant. Under this context, we can expect that materials with a stronger spin-orbit interaction like germanene and transition metal dichalcogenides could result in steeper conductance characteristics and consequently better thermoelectric properties. These materials could also help to have a greater energy range for the operation of thermoelectric devices.

In third place, we want to contrast our results with the available literature. In particular, we consider instructive a comparison between silicene and graphene superlattices. The case of graphene superlattices has previously been studied from a theoretical stand point.[32] We can notice that in general the results are qualitatively similar for both systems; however, there are important quantitative differences. For instance, in silicene superlattices, the Seebeck coefficient derived from the oscillating conductance reaches a maximum value of 4 mV/K, while in graphene superlattices the same coefficient has a maximum value of roughly 0.3 mV/K, that is, the values obtained in the present work are one order of magnitude higher. In the case of the power factor, we have calculated a maximum value of 5 nW/K^2, in contrast to the maximum obtained in 8-period graphene superlattices of approximately 5 pW/K^2, so our value is three orders of magnitude higher. To carry out this comparison, we have divided the Seebeck coefficient of graphene superlattices by a factor of 6 because the temperature in that case was 300 K. Likewise, we multiply the conductance by a factor of 2 to account the contribution of the *K*' valley. Regarding experimental works, there are important contributions trying to unveil the thermoelectric response of graphene.[41,51] However, as far as we know there are no experimental reports about gated graphene and/or silicene superlattices. So, we will try to contrast our results with the mentioned experimental ones of pristine graphene. In the case of the thermoelectric power (TEP) or Seebeck coefficient, the values obtained for graphene and silicene superlattices are larger than the reported ones in the referred experimental works. For instance, the maximum TEPs for graphene and silicene superlattices were 0.3 mV/K and 4 mV/K, while for graphene on hBN (G/hBN) the maximum TEP was 182 μV/K.[51] This is consistent with the idea that nanostructuring a material, that is, redistributing the density of states, the thermoelectric properties can be improved. It is also important to remark that the physical origin of the maximum values in superlattices is quite different with respect to G/hBN and G/SiO_2.[41,51] In the latter, the electron-hole puddles formed by the substrate random potential fluctuations are directly involved in the maximization of the TEP. In the former, the conductance oscillations associated with the redistribution of the density of states are the reason of the TEP improvement. Furthermore, the type of transport is quite different, while in G/hBN or G/SiO_2 we are talking about diffusive transport, sample sizes and scattering mechanisms, in superlattices we are dealing with coherent quantum transport. In the case of the power factor, we cannot make a direct comparison because for G/hBN the conductivity is reported in units of S/cm rather than in S, the typical unit for a 2D material like graphene, see the seminal work of Novoselov *et al.*[52] In fact, to relate conductivity and conductance the cross section of the device is necessary; however, as far as we corroborate, this information is not available in the experimental report.[51] At this point, it is important to mention that in principle we are dealing with high quality graphene, at least a graphene that assures ballistic transport. Therefore, the conductivity that we are reporting is of the order or even better than that reported in the experimental works. Under these circumstances, we expect that the enhancement of the power factor be proportional to the rise of the TEP.

Finally, we want to address an important quantity like the thermal conductivity. Its relevance lies in its direct relation to the figure of merit and consequently to the efficiency of the thermoelectric devices. To this repect, it is known that the thermal conductivity of silicene is mostly given by phonons. However, as far as we know, it has not been possible to make experimental measurements of thermal conductivity due to the challenges involved in synthesizing freestanding silicene. In contrast, many theoretical studies of phonon transport in silicene have been carried out by employing two principal numerical simulation techniques: the classical Molecular Dynamics (MD)[53] and the first principles method.[54] The reported values of thermal conductivity are in the range of 5-65 W/mK, lower than suspended graphene,[55] 3000-5000 W/mK. The big difference is that in graphene the flexural phonons corresponding to acoustic out-plane vibration modes contribute more than 50% to the thermal conductivity,[56] while in silicene contribute less than 10%,[57] and the thermal transport is dominated mostly (90%) by in-plane longitudinal phonon modes. The low-buckled lattice of silicene breaks the reflection symmetry causing a strong out-plane phonon scattering. In addition, it has been found that the thermal conductivity of graphene and silicene could be modulated depending on the substrate where they are deposited.[58,59] For instance, it is reported that graphene nanoribbons (GNRs) supported on silicon dioxide (SiO_2) have a low thermal conductivity,[60] ~80 W/mK at 300 K. The enormous reduction is due to the fact that the contact of the graphene sheet with the surface of the substrate affects the flexural phonon modes limiting its movement of vibration. In the same direction, a theoretical study of silicene suspended on amorphous SiO_2 was carried out, resulting in a reduction up to 78% of the thermal conductivity at 300 K.[61] Even better, by applying an external electric field along the upward out-of-plane direction, the thermal conductivity of silicene can be reduced up to two orders of magnitude of its suspended value.[62] This is very important for us, since in our device, the gated structure is created through the application of external electric field along the perpendicular direction to the silicene layer. In short, the effect of the reduction of the thermal conductivity, combined with the increased values of the power factor obtained in this work, allows us to think in an improvement of the figure of merit of up to two orders of magnitude with respect to GGSLs. This reinforces the idea that silicene could be a good option for its implementation in more efficient thermoelectric devices.

V. CONCLUSIONS

In summary, we show that low-dimensional thermoelectricity in silicene could be a good option to improve the performance and efficiency of thermoelectric devices. The natural redistribution of the electron density of states in gated silicene superlattices in conjunction with the intrinsic characteristics of the material, local bandgap, and large spin-orbit coupling, give rise to a significant improvement of the thermoelectric properties. A Dirac-like Hamiltonian was used to describe silicene electrons. The transfer matrix approach, the Landauer-Büttiker formalism, and the Cutler-Mott formula were used to obtain the transmission, transport, and thermoelectric properties, respectively. We find that the conductance has a steeper oscillating trend than in graphene. This characteristic gives rise to Seebeck coefficients and power factors of the order of mV/K and nW/K^2, respectively. These large values of the power factor in combination with the low thermal conductivity of silicene could be the base for better figures of merit. This is even more relevant if we consider that the thermal conductivity is further reduced by supporting substrates or the application of an external perpendicular electric field. In fact, fundamental structural conditions of gated silicene superlattices give the possibility of manipulating in a controlled way the electronic transport, and consequently, the thermoelectric properties.

ACKNOWLEDGMENTS

This work was partially supported by Grant No. 252677 from CONACyT and No. PAPIIT-IN104616 from UNAM, Mexico. E.J.G. thanks CONACyT for a Ph.D. fellowship.

[1]A. H. Castro Neto, F. Guinea, N. M. R. Peres, K. S. Novoselov, and A. K. Geim, Rev. Mod. Phys. **81**, 109 (2009).
[2]S. Das Sarma, S. Adam, E. H. Hwang, and E. Rossi, Rev. Mod. Phys. **83**, 407 (2011).
[3]V. Singh, D. Joung, L. Zhai, S. Das, S. I. Khondaker, and S. Seal, Prog. Mater. Sci. **56**, 1178 (2011).
[4]K. Takeda and K. Shiraishi, Phys. Rev. B **50**, 14916 (1994).
[5]G. G. Guzmán-Verri and L. C. Lew Yan Voon, Phys. Rev. B **76**, 075131 (2007).
[6]S. Cahangirov, M. Topsakal, E. Aktürk, H. Şahin, and S. Ciraci, Phys. Rev. Lett. **102**, 236804 (2009).
[7]C.-C. Liu, W. Feng, and Y. Yao, Phys. Rev. Lett. **107**, 076802 (2011).
[8]L. Chen, C.-C. Liu, B. Feng, X. He, P. Cheng, Z. Ding, S. Meng, Y. Yao, and K. Wu, Phys. Rev. Lett. **109**, 056804 (2012).
[9]C.-C. Liu, H. Jiang, and Y. Yao, Phys. Rev. B **84**, 195430 (2011).
[10]M. Ezawa, Phys. Rev. B **87**, 155415 (2013).
[11]O. Oubram, O. Navarro, E. J. Guzmán, and I. Rodríguez-Vargas, Superlattices Microstruct. **113**, 483 (2018).
[12]Y. Wang and Y. Lou, J. Appl. Phys. **114**, 183712 (2013).
[13]F. Liu, C.-C. Liu, K. Wu, F. Yang, and Y. Yao, Phys. Rev. Lett. **111**, 066804 (2013).
[14]C. Forman, I. K. Muritala, R. Pardemann, and B. Meyer, Renew. Sustain. Energy Rev. **57**, 1568 (2016).
[15]D. M. Rowe, *CRC Handbook of Thermoelectrics* (CRC Press, 1995).
[16]G. S. Nolas, J. W. Sharp, and H. J. Goldsmid, *Thermoelectrics: Basic Principles and New Materials Developments* (Springer, Berlin, 2001).
[17]A. F. Ioffe, *Semiconductors Thermoelements and Thermoelectric Cooling* (Infosearch, London, 1957).
[18]A. Bejan and A. D. Kraus, *Heat Transfer Handbook* (Wiley, New York, 2003).
[19]L. D. Hicks and M. S. Dresselhaus, Phys. Rev. B **47**, 12727 (1993).
[20]M. Dresselhaus, G. Chen, M. Tang, R. Yang, H. Lee, D. Wang, Z. Ren, J. Fleurial, and P. Gogna, Adv. Mater. **19**, 1043 (2007).
[21]K.-X. Chen, M.-S. Li, D.-C. Mo, and S.-S. Lyu, Front. Energy **12**, 97 (2018).
[22]J. He and T. M. Tritt, Science **357**, 1369 (2017).
[23]P. Dollfus, V. H. Nguyen, and J. Saint-Martin, J. Phys. Condens. Matter **27**, 133204 (2015).
[24]K. Zberecki, M. Wierzbicki, J. Barnaś, and R. Swirkowicz, Phys. Rev. B **88**, 115404 (2013).
[25]L. Pan, H. J. Liu, X. J. Tan, H. Y. Lv, J. Shi, X. F. Tang, and G. Zheng, Phys. Chem. Chem. Phys. **14**, 13588 (2012).
[26]H. Sadeghi, S. Sangtarash, and C. J. Lambert, Sci. Rep. **5**, 9514 (2015).
[27]K. Yang, S. Cahangirov, A. Cantarero, A. Rubio, and R. D'Agosta, Phys. Rev. B **89**, 125403 (2014).
[28]D. Dragoman and M. Dragoman, Appl. Phys. Lett. **91**, 203116 (2007).
[29]M. Cheng, Phys. E: Low-dimen. Syst. Nanostruct. **46**, 189 (2012).
[30]S. Kumar Mishra, A. Kumar, C. Prakash Kaushik, and B. Dikshit, J. Appl. Phys. **121**, 184301 (2017).
[31]S. K. Mishra, A. Kumar, C. P. Kaushik, and B. Dikshit, Mater. Res. Express **5**, 016301 (2018).
[32]S. Molina-Valdovinos, J. Martínez-Rivera, N. E. Moreno-Cabrera, and I. Rodríguez-Vargas, Phys. E: Low-dimen. Syst. Nanostruct. **101**, 188 (2018).
[33]B. Aufray, A. Kara, S. Vizzini, H. Oughaddou, C. Léandri, B. Ealet, and G. L. Lay, Appl. Phys. Lett. **96**, 183102 (2010).
[34]B. Lalmi, H. Oughaddou, H. Enriquez, A. Kara, S. Vizzini, B. Ealet, and B. Aufray, Appl. Phys. Lett. **97**, 223109 (2010).
[35]C. Léandri, H. Oughaddou, B. Aufray, J. M. Gay, G. L. Lay, A. Ranguis, and Y. Garreau, Surf. Sci. **601**, 262 (2007).
[36]L. Meng, Y. Wang, L. Zhang, S. Du, R. Wu, L. Li, Y. Zhang, G. Li, H. Zhou, W. A. Hofer, and H.-J. Gao, Nano Lett. **13**, 685 (2013).
[37]A. Fleurence, R. Friedlein, T. Ozaki, H. Kawai, Y. Wang, and Y. Yamada-Takamura, Phys. Rev. Lett. **108**, 245501 (2012).
[38]D. Chiappe, E. Scalise, E. Cinquanta, C. Grazianetti, B. van den Broek, M. Fanciulli, M. Houssa, and A. Molle, Adv. Mater. **26**, 2096 (2014).
[39]L. Tao, E. Cinquanta, D. Chiappe, C. Grazianetti, M. Fanciulli, M. Dubey, A. Molle, and D. Akinwande, Nat. Nanotechnol. **10**, 227 (2015).
[40]M. Cutler and N. F. Mott, Phys. Rev. **181**, 1336 (1969).
[41]Y. M. Zuev, W. Chang, and P. Kim, Phys. Rev. Lett. **102**, 096807 (2009).
[42]A. F. Young and P. Kim, Nat. Phys. **5**, 222 (2009).
[43]L. Wang, I. Meric, P. Y. Huang, Q. Gao, Y. Gao, H. Tran, T. Taniguchi, K. Watanabe, L. M. Campos, D. A. Muller, J. Guo, P. Kim, J. Hone, K. L. Shepard, and C. R. Dean, Science **342**, 614–617 (2013).
[44]Y. Wang, D. Wong, A. V. Shytov, V. W. Brar, S. Choi, Q. Wu, H.-Z. Tsai, W. Regan, A. Zettl, R. K. Kawakami, S. G. Louie, L. S. Levitov, and M. F. Crommie, Science **340**, 734–737 (2013).
[45]S. Chen, Z. Han, M. M. Elahi, K. M. M. Habib, L. Wang, B. Wen, Y. Gao, T. Taniguchi, K. Watanabe, J. Hone, A. W. Ghosh, and C. R. Dean, Science **353**, 1522–1525 (2016).
[46]B. Terrés, L. A. Chizhova, F. Libisch, J. Peiro, D. Jörger, S. Engels, A. Girschik, K. Watanabe, T. Taniguchi, S. V. Rotkin, J. Burgdörfer, and C. Stampfer, Nat. Commun. **7**, 11528 (2016).
[47]Z.-G. Shao, X.-S. Ye, L. Yang, and C.-L. Wang, J. Appl. Phys. **114**, 093712 (2013).
[48]N. M. R. Peres, Rev. Mod. Phys. **82**, 2673–2700 (2010).
[49]H.-Z. Lu, W. Yao, D. Xiao, and S.-Q. Shen, Phys. Rev. Lett. **110**, 016806 (2013).
[50]V. V. Cheianov and V. I. Fal'ko, Phys. Rev. B **74**, 041403 (2006).
[51]J. Duan, X. Wang, X. Lai, G. Li, K. Watanabe, T. Taniguchi, M. Zebarjadi, and E. Y. Andrei, Proc. Natl. Acad. Sci. U.S.A. **113**, 14272–14276 (2016).
[52]K. S. Novoselov, A. K. Geim, S. V. Morozov, D. Jiang, Y. Zhang, S. V. Dubonos, I. V. Grigorieva, and A. A. Firsov, Science **306**, 666–669 (2004).
[53]X. Zhang, H. Xie, M. Hu, H. Bao, S. Yue, G. Qin, and G. Su, Phys. Rev. B **89**, 054310 (2014).
[54]X. Gu and R. Yang, J. Appl. Phys. **117**, 025102 (2015).
[55]A. A. Balandin, S. Ghosh, W. Bao, I. Calizo, D. Teweldebrhan, F. Miao, and C. N. Lau, Nano Lett. **8**, 902 (2008).
[56]L. Lindsay, D. A. Broido, and N. Mingo, Phys. Rev. B **82**, 115427 (2010).
[57]H. Xie, M. Hu, and H. Bao, Appl. Phys. Lett. **104**, 131906 (2014).
[58]W. Cai, A. L. Moore, Y. Zhu, X. Li, S. Chen, L. Shi, and R. S. Ruoff, Nano Lett. **10**, 1645 (2010).
[59]X. Zhang, H. Bao, and M. Hu, Nanoscale **7**, 6014 (2015).
[60]A. D. Liao, J. Z. Wu, X. Wang, K. Tahy, D. Jena, H. Dai, and E. Pop, Phys. Rev. Lett. **106**, 256801 (2011).
[61]Z. Wang, T. Feng, and X. Ruan, J. Appl. Phys. **117**, 084317 (2015).
[62]G. Qin, Z. Qin, S.-Y. Yue, Q.-B. Yan, and M. Hu, Nanoscale **9**, 7227 (2017).